Check for updates

ChemCatChem

Research Article
doi.org/10.1002/cctc.202301324

Chemistry Europe
European Chemical Societies Publishing

www.chemcatchem.org

Bifunctional Substrates: *In-situ* Ni, Fe co-doped Cobalt Carbonate Hydroxides for Overall Water Splitting

Yiqing Sun[+],[a] Xiongyi Liang[+],[b] Di Yin,[b] Yuxuan Zhang,[b] Dong Chen,[b] Kaihang Yue,[a] Ziyan Cai,[a] Xiuming Bu,*[a] Xianying Wang,*[a] and Johnny C. Ho*[b, c]

Developing highly efficient and stable electrocatalysts with large current densities for hydrogen and oxygen evolution is still challenging. Herein, Ni and Fe co-doped cobalt carbonate hydroxide catalysts were designed *in situ* on the three-dimensional porous NiFe foam through a facile one-step hydrothermal strategy. Inductively coupled plasma atomic emission spectrum, transmission electron microscopy-element mapping, X-ray photoelectron spectroscopy, and DFT calculations demonstrate that the three-dimensional NiFe foam substrate not only serves as the porous substrate, which enhances the exposed number of active sites, but also enhances the intrinsic activities of single active sites *via* introducing Ni and Fe dopants in the cobalt carbonate hydroxide catalyst during the hydrothermal process. The obtained hybrid electrocatalyst can be employed as a highly efficient and stable bifunctional electrocatalyst for the oxygen and hydrogen evolution reactions, with overpotentials of 340 mV and 371 mV at 1000 mA cm^{-2}, respectively. In addition, tests in an alkaline electrolyzer revealed that the current density could reach 1000 mA cm^{-2} at a voltage of 2 V and maintain stable operation for 100 h.

1. Introduction

The massive fossil energy consumption yields severe environmental pollution problems, necessitating the search for clean sources.[1,2] Electrochemical water splitting is widely considered a probable pathway to address the above problems by employing renewable electricity to convert water into hydrogen and oxygen.[3,4] Although noble metals such as Pt and Ru-based materials are deemed the most active electrocatalysts for the water splitting reaction, cost and scarcity limited their practical application.[5,6] It is thus critically urgent to explore and design earth-abundant, low-cost, and highly effective non-noble metal electrocatalysts for overall water splitting. Especially, the large current densities >1000 mA cm^{-2} with high stability are necessary for the practical application.[7–10] Therefore, designing efficient non-noble metal-based electrocatalysts with larger current densities is still challenging.

After several decades of investigations on the electrocatalysts, the electrochemical performance is mainly governed by the number of expose active sites and intrinsic activities of each site.[11] Bearing this in mind, heteroatom doping is frequently employed as a technique to modify the electronic configuration of the active sites at the atomic level, thereby optimizing the adsorption/desorption ability between the active sites and intermediate products ultimately achieving the goal of improving the intrinsic activities enhanced electrocatalytic performance.[12–15] Normally, there are two main methods for heteroatom doping in the electrocatalyst community, including the liquid phase method (introduction of heteroatom-containing precursors in the mixture solution) and the gas phase method (introduction of heteroatom-containing active gas at high temperature).[16–19] Another attractive method is the direct preparation of catalysts on the three-dimensional (3D) porous and conductive substrate (*e.g.*, nickel foam, nickel-iron foam, carbon cloth, *etc.*), which can not only increase the contact between the catalyst and the substrate, but also to ensure the stability current, at the same time can improve the exposed quantity of the active sites per unit volume.[20–22] Very recently, we investigated the corrosion and redeposition behavior of the nickel foam in different situations during the hydrothermal process under various conditions, such as distilled water, urea, Fe^{3+}, Fe^{2+}, Co^{2+}, and Mn^{2+}. The result clearly proves the nickel atoms in the nickel foam substrate will dissolve in the solution and then deposit onto the surface of the substrate accompanied by the precursors, thus affecting their electrochemical characteristics. Meanwhile, the solubility of nickel ions in solution has a positive relationship with reaction temperature since metal ion hydrolysis is an endothermic reaction. Therefore, based on our previous results, it is reasonable to expect that the composition of the catalyst can be tailored by adjusting the concentration of escaping ions from the substrate without adding additional dopant precursors, which would in turn enhance the performance.

Herein, a straightforward one-step hydrothermal method was employed to prepare Ni and Fe co-doped cobalt carbonate

[a] *Y. Sun,[+] K. Yue, Z. Cai, X. Bu, X. Wang*
CAS Key Laboratory of Materials for Energy Conversion, Shanghai Institute of Ceramics, Chinese Academy of Sciences (SICCAS), Shanghai 200050, P.R. China
E-mail: buxiuming@mail.sic.ac.cn
wangxianying@mail.sic.ac.cn

[b] *X. Liang,[+] D. Yin, Y. Zhang, D. Chen, J. C. Ho*
Department of Materials Science and Engineering, City University of Hong Kong, Kowloon 999077, Hong Kong SAR, P.R. China
E-mail: johnnyho@cityu.edu.hk

[c] *J. C. Ho*
State Key Laboratory of Terahertz and Millimeter Waves, City University of Hong Kong, Kowloon 999077, Hong Kong SAR, P.R. China

[+] *Contributed equally to this work.*

Supporting information for this article is available on the WWW under https://doi.org/10.1002/cctc.202301324

© 2023 Wiley-VCH GmbH

hydroxides *in situ* on the three-dimensional (3D) porous nickel iron (NiFe) foam. Inductively coupled plasma atomic emission spectrum, transmission electron microscopy-element mapping, and X-ray photoelectron spectroscopy demonstrate the successful introduction of Ni and Fe dopants on the cobalt carbonate hydroxide catalyst. More importantly, the morphology and dopant concentration of the cobalt carbonate hydroxide can be simultaneously modified by optimizing the processed temperature, which can enhance the active sites' exposed active surface area and intrinsic activity, respectively. As a result, the developed Ni and Fe co-doped cobalt carbonate/NiFe electrode shows superior OER and HER bifunctional electrocatalytic performance, exhibiting overpotentials of 340 mV and 371 mV at 1000 mA cm^{-2}, respectively. In addition, another alkaline electrolyzer was also built capable of sustaining a current density of 1000 mA cm^{-2} at approximately 2 V over 100 h of long-term operation. The outstanding electrolytic performance suggests that Ni and Fe co-doped cobalt carbonate/NiFe electrodes have potential practical applications in overall water splitting. Moreover, our research provides experimental evidence for the significant impact of substrate on the target catalyst during the hydrothermal process, which introduces a novel approach for catalyst performance modification.

2. Materials and methods

2.1. Preparation of Ni and Fe co-doped cobalt carbonate hydroxides nanowires on nickel-iron foam

In this study, all of the nickel-iron foam (molar ratio of Ni to Fe is 7 : 3) underwent the following treatments: acetone treatment, HCl (2 M), distilled water treatment, and ethonal treatment for 10 min, respectively. The preparation process of Ni and Fe co-doped cobalt carbonate hydroxide (CCH) nanowires on the nickel-iron foam was according to previous work with a slight modification. Typically, 1 mmol $Co(NO_3)_2 \cdot 6H_2O$ and 250 mg hexamethylenetetramine were added into 10 mL deionized water. The homogenous solution and a piece of NiFe foam were then enclosed in a Teflon-coated stainless steel autoclave, then the autoclave was heated in an electric oven at 160 °C for 8 h. After allowing the material to cool to room temperature naturally, the resulting nickel iron foam covered with nanowires (CCH/NFF-160) was thoroughly rinsed with with deionized water and ethanol using ultrasound. The material was then dried overnight in a vacuum oven at 60 °C. For comparison, the samples CCH/NFF-180 and CCH/NFF-200 were prepared according to the above preparation procedures and except changing the hydrothermal treatment's temperature to 180 °C and 200 °C, respectively. Pure cobalt carbonate hydroxides (CCH) were also prepared with the same process except adding the substrate.

Meanwhile, the CCH on the Ni plate, Fe plate, Ni foam and Fe foam were also obtained with the above preparation process, excepting replacing the NiFe foam substrate with the Ni plate, Fe plate, Ni foam and Fe foam.

2.2. Material characterization

Bruker D2 Phaser fitted with the monochromatized Cu-Kα radiation was used to check the purity and crystalline structure of the samples. Field emission scanning electron microscopy (SU-8010, Hitachi, Tokyo, Japan) was used to evaluate the morphology and dimensions of the samples. A Tecnai G2 F30 (FEI, Hillsboro, OR, USA) with an accelerating voltage of 200 kV was used for transmission electron microscopy (TEM) and high-resolution transmission electron microscopy (HRTEM). The metal ions concentration was investigated by inductively coupled plasma atomic emission spectrometry. X-ray photoelectron spectroscopy (XPS) was conducted on an ESCALAB 250 XI X-ray photoelectron spectrometer and Thermo Fisher Scientific K-Alpha (Thermo Scientific Co., USA) with Al Kα radiation.

2.3. Electrochemical measurement

The Gamry 300 electrochemical workstation, equipped with a typical three-electrode setup, was used for all electrochemical characterizations at room temperature. A saturated calomel electrode (SCE), a carbon rod, and the prepared electrocatalysts were employed as the reference, counter, and working electrodes, respectively. For the OER and HER experiments, liner sweep voltammetry (LSV) curves were measured at a scanning rate of 5 mV s^{-1}. The potential (versus SCE) was converted into RHE values using the following equation: $E_{RHE} = E_{SCE} + 0.2415 + 0.059 \times pH$. To maintain a stable electrode surface, multiple cycles of cyclic voltammetry (CV) were performed before evaluating its electrochemical activity, until the hydrogen precipitation current exhibited negligible variations. All voltammograms were automatically recorded on the workstation with iR drop compensation, unless indicated otherwise.

2.4. Density Functional Theory (DFT) Calculations

The Perdew-Burke-Ernzerhof (PBE) functional was chosen to characterize the exchange-correlation interaction. The calculations using spin-polarized density functional theory (DFT) were carried out by Quantum Espresso with the implementation of projector-augmented wave (PAW) potentials.[23,24] The DFT + U calculations were used to determine the strong on-site Coulomb interaction of the localized electrons. The kinetic energy cut-offs for the wave functions and the density were 40 Ry and 500 Ry, respectively, as given by standard solid-state pseudopotentials.[25,26] The Hubbard correction U for the 3d orbitals of Co, Ni and Fe was objectively set to 3.32, 6.20 and 5.30 eV respectively. Grimme's DFT-D3 method was used to account for van der Waals (vdW) interactions,[27] with a convergence threshold of 0.02 eV/Å for total energy and 10^{-5} eV for total force. Technical terms were explained when first used. A 4×4×3 supercell of 240 atoms was constructed and the gamma point was used to sample the Brillouin zone to model different metal atom ratios.

© 2023 Wiley-VCH GmbH

18673899, 2024, 4, Downloaded from https://chemistry-europe.onlinelibrary.wiley.com/doi/10.1002/cctc.202301324 by City Universitaet Of Hong Kong, Wiley Online Library on [05/03/2024]. See the Terms and Conditions (https://onlinelibrary.wiley.com/terms-and-conditions) on Wiley Online Library for rules of use; OA articles are governed by the applicable Creative Commons License

3. Results and Discussion

According to our previous report, the corrosion degree of the Ni foam substrate increases with increasing temperature during the hydrothermal reaction, which can be attributed to the hydrolysis of the precursors and/or oxidation reaction between the precursor and substrate. Therefore, it is feasible to control the ratio of cation doping in the target catalyst by adjusting the processing temperature. Herein, we selected 3D NiFe foam as the substrate commercially available at low cost.[20] The scanning electron microscope (SEM) image of bare NiFe foam with a continuous three-dimensional (3D) porous structure are shown in Figure S1. Inductively coupled plasma (ICP) atomic emission spectrometry confirmed the atom ratio of nickel to iron is 7 to 3. Three different kinds of cobalt carbonate hydroxide (CCH) based samples were prepared on the surface of the NiFe foam *via* changing treatment temperature of the hydrothermal reaction, including CCH/NFF-160 (160 °C), CCH/NFF-180 (180 °C) and CCH/NFF-200 (200 °C). The effect of temperature on the structure and composition was first investigated by X-ray diffraction (XRD). As shown in Figure 1, with the exception of the peaks identified as NiFe foam (indicated by a hashtag), the samples prepared at 160 °C and 180 °C both exhibit characteristic peaks indexed to cobalt carbonate hydroxides (JCPDS NO. 48–0084, marked with an asterisk).[22] While the sample is prepared at 200 °C, in addition to the characteristic peaks of CCH, new sharp peaks at 11.6° and 23.2° can be observed, which can be assigned to the diffraction of $Ni(OH)_2$ (JCPDS NO. 22–0444, marked with a circle). Since the hydrolysis of Co^{2+} is an endothermic reaction ($Co^{2+} + 2H_2O \rightleftharpoons Co(OH)_2 + 2H^+$, $\triangle H > 0$), the rise in temperature promotes the hydrolysis reaction to move forward, leading to an elevated concentration of H^+. Then, the substrate reacts with the H^+ to release a significant quantity of Ni ions and a minor quantity of Fe ions in the solution mixture. Therefore, the abundant Ni^{2+} ion will form a new phase with the assistance of hexamethylenetetramine.

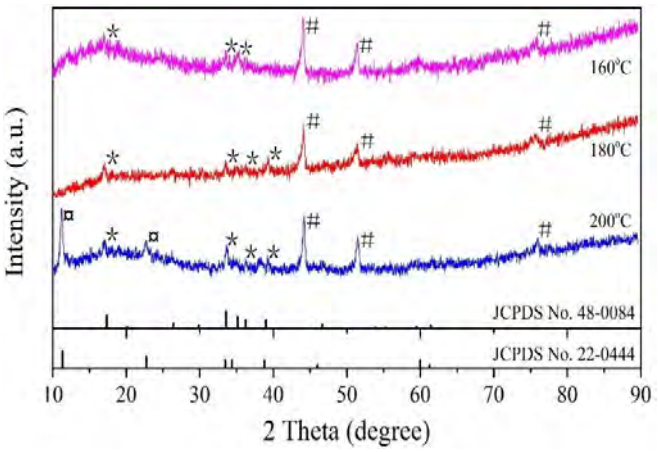

Figure 1. XRD patterns of the cobalt carbonate hydroxide (CCH) samples, including CCH/NFF-160, CCH/NFF-180, and CCH/NFF-200. The peaks labelled with a hashtag, asterisk, and circle are indexed to NiFe foam, CCH, and $Ni(OH)_2$, respectively.

Then, the morphology of these samples was investigated using SEM and TEM, as shown in Figure 2. Figure 2a and 2b exhibit that the needle-like nanowires, approximately 20 μm in length, grew evenly on the NiFe substrate when heated to 160 °C. The TEM and HRTEM images in Figure 2c show the lattice fringe of 0.27 nm, which refers to the CCH (221) facet. Energy-dispersive X-ray spectroscopy (EDX) mapping was employed to identify the elements and visualize the distributions in the CCH/NFF-160 (Figure 2d). Co, Fe, and Ni elements are detected with uniform distribution on the nanowire. Moreover, the point mode in EDX was used to detect the atomic ratio of different components on the catalyst surface. The result shows that the atomic ratio between Co, Ni, and Fe are 95.64 ± 0.35 %, 3.08 ± 0.35 %, and 1.28 ± 0.35 %, indicating that the corrosion behavior of NiFe foam has occurred during the hydrothermal process. However, because of the large detection depth (about hundreds of nanometers to micrometers) and low sensitivity of the EDX characterization technique, the proportion data of nickel and iron atoms collected is higher than that in the catalyst lattice, which may be mainly due to surface physical absorption. It should be noticed here that the presence of Fe ions is not only due to the hydrolysis reaction as discussed above but also to the redox reaction between the Co^{2+} ion and Fe metal in the NiFe substrate. After increasing the temperature to 180 °C, CCH/NFF-180 exhibits a similar nanowire structure to the CCH/NFF-160 (Figure 2e and 2f). The HRTEM and element analysis of the CCH/NFF-180 in Figure 2g and 2h confirm the NiFe corrosion behavior again. Compared with the EDX point mode results of the CCH/NFF-160, the atomic ratio of Ni and Fe in the CCH/NFF-180 is greatly increased, and the atomic ratio between Co, Ni, and Fe are 90.67 ± 0.21 %, 7.72 ± 0.21 %, and 1.61 ± 0.21 %. While increasing temperature, the CCH/NFF-200 nanowires come together and become sparse, implying a decreased exposed area of active sites (Figure 2i). These results demonstrated that the process temperature obviously affects the morphologies of the CCH nanowires. More importantly, in contrast to the smooth surface of the CCH/NFF-160 and CCH/NFF-180 nanowires, dense nanosheets were wrapped on the nanowire surface, as shown in Figure 2j. The HRTEM image confirms the layer structure of the nanosheets (~8 layers) and a lattice spacing of 0.25 nm (equivalent to the $Ni(OH)_2$ (111) plane), in agreement with the XRD results (Figure 2k). Meanwhile, the atomic ratio of Ni increases exponentially, and the atomic ratio between Co, Ni, and Fe reaches 78.39 ± 0.75 %, 19.60 ± 0.75 %, and 2.01 ± 0.75 % (summarized EDX data shown in Table S1). The obviously increased concentration of Ni and Fe ions on the catalyst's surface suggests that the temperature increasement accelerates the corrosion behavior of the NiFe substrate during the hydrothermal process and proves the possible heteroatom doping in the CCH catalyst.

As discussed above, the high atomic ratio of Ni and Fe ions on the catalyst surface may be mainly due to surface physical absorption because of the limitations of the EDX characterization technique. Therefore, to further confirm the influence of NiFe substrate on the CCH catalyst electronic structure, XPS was utilized to examine the chemical valence of Ni, Fe, and Co in these catalysts, respectively. As shown in Figure 3a, Ni $2p_{3/2}$ can

© 2023 Wiley-VCH GmbH

18673899, 2024, 4, Downloaded from https://chemistry-europe.onlinelibrary.wiley.com/doi/10.1002/cctc.202301324 by City Universitaet Of Hong Kong, Wiley Online Library on [05/03/2024]. See the Terms and Conditions (https://onlinelibrary.wiley.com/terms-and-conditions) on Wiley Online Library for rules of use; OA articles are governed by the applicable Creative Commons License

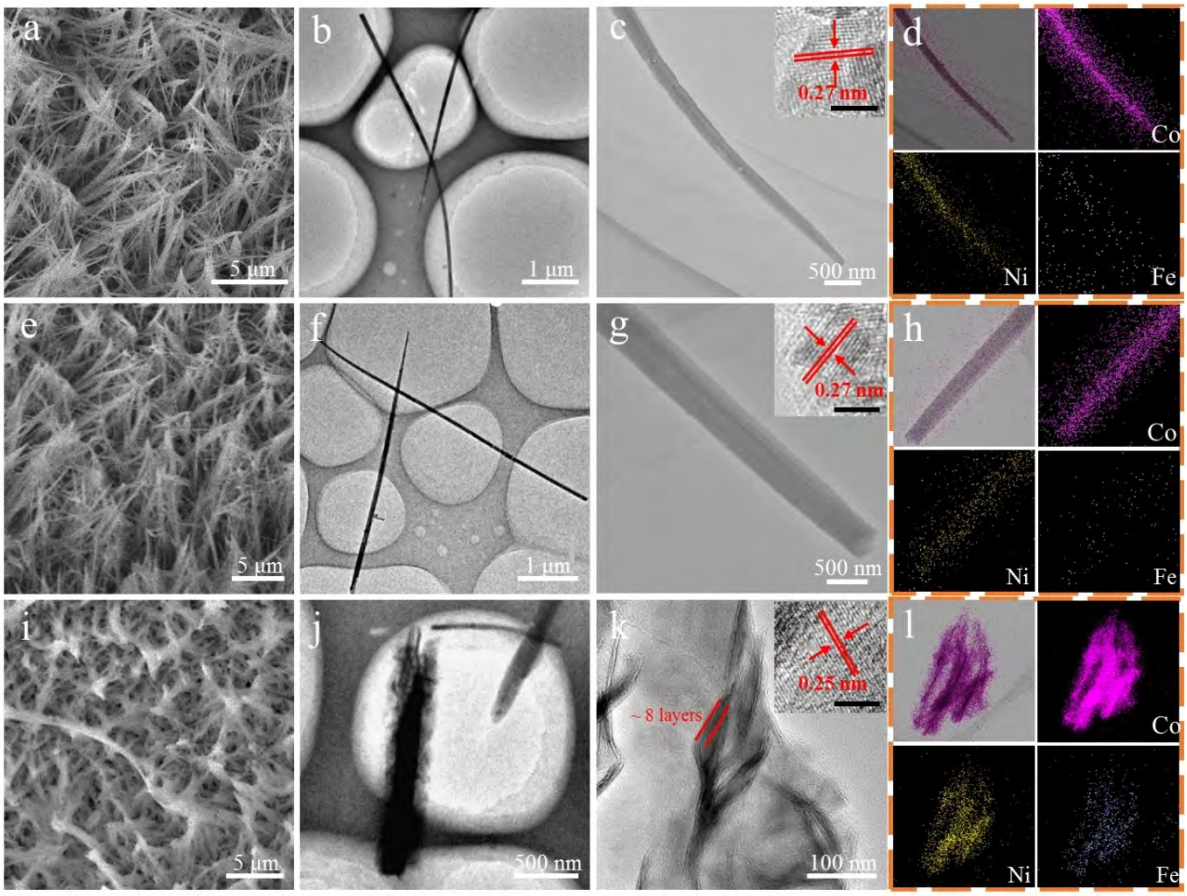

Figure 2. (a) SEM image, (b, c) TEM images, and (d) corresponding element mapping of CCH-160, the inset of (c) is the HRTEM image; (e) SEM image, (f, g) TEM images and (h) corresponding element mapping of CCH-180, the inset of (g) is the HRTEM image; (i) SEM image, (j, k) TEM images and (l) corresponding element mapping of CCH-200. The scale bars in the inset panels c, g, and k are 2 nm.

be deconvoluted into three peaks: the Ni^{2+} peak at 854.5 eV, the Ni^{3+} peak at 855.6 eV, and the satellite peak at 860.9 eV.[28] Compared with the original NiFe substrate, the increased binding energy of Ni $2p_{3/2}$ and the Ni^{2+}/Ni^{3+} ratio were observed after hydrothermal treatment, indicating the change of the chemical environment and thus proving Ni is involved in the deposition of the catalyst on the surface of the substrate during the hydrothermal reaction.[29] The binding energy of Fe shows a similar trend as shown in Figure S2. Then, the electron structures of the main active sites of Co were investigated, as presented in Figure 3b. The ratio between Co^{3+} and Co^{2+} increases significantly with the increasing process temperature. Since there are two variable parameters in this experiment, involving the temperature change and the corresponding concentration change of the heteroatom, the change in the chemical valence of Co can be attributed to temperature increase and/or heteroatom doping. Thus, to check the influence of temperature changes on the electron structure of Co, a series of CCH samples were synthesized at different hydrothermal temperatures without adding NiFe substrate, including CCH-160 (160 °C), CCH-180 (180 °C) and CCH-200 (200 °C). As compiled in Figure 3c, the position and area of the peaks are almost unchanged among these CCH samples. This observation confirms that the electronic structure changes of Co atoms in the CCH/NiFe composite result from heteroatom doping, consistent with the previous report.[30] Combined with the EDX data and XPS analysis, most of the Ni and Fe ions in the solution are adsorbed on the catalyst's surface, and only a small part is doped into the crystal lattice of the CCH catalyst. In addition, a more accurate atomic ratio between Ni, Fe and Co was also collected via XPS technique due to a smaller detection depth than that of EDX, as shown in Table S2. This way, the chemical composition of CCH/NFF-160 and CCH/NFF-180 are determined to be Ni and Fe co-doped CCH/NFF, while CCH/NFF-200 consists of the Co and Fe co-doped $Ni(OH)_2$, and Ni and Fe co-doped CCH hybrid/NFF.

Meanwhile, the projected density of states (PDOS) of main active sites (*i.e.*, Co in the pure CCH and CCH/NFF-180) were calculated, as shown in Figure 3d. The intercalated carbonate anions in the samples were excluded, and the characterized structures are shown in Figure S3 and Table S3. Obviously, the valance band and conduction band position move down in the CCH/NFF-180, indicating the d band center of CCH/NFF-180 is farther away from the Fermi level than the original CCH.[31,32] Previous reports have demonstrated that the downshift of the d band center in CCH catalysts may lower the adsorption energy

© 2023 Wiley-VCH GmbH

18673899, 2024, 4, Downloaded from https://chemistry-europe.onlinelibrary.wiley.com/doi/10.1002/cctc.202301324 by City Universitaet Of Hong Kong, Wiley Online Library on [05/03/2024]. See the Terms and Conditions (https://onlinelibrary.wiley.com/terms-and-conditions) on Wiley Online Library for rules of use; OA articles are governed by the applicable Creative Commons License

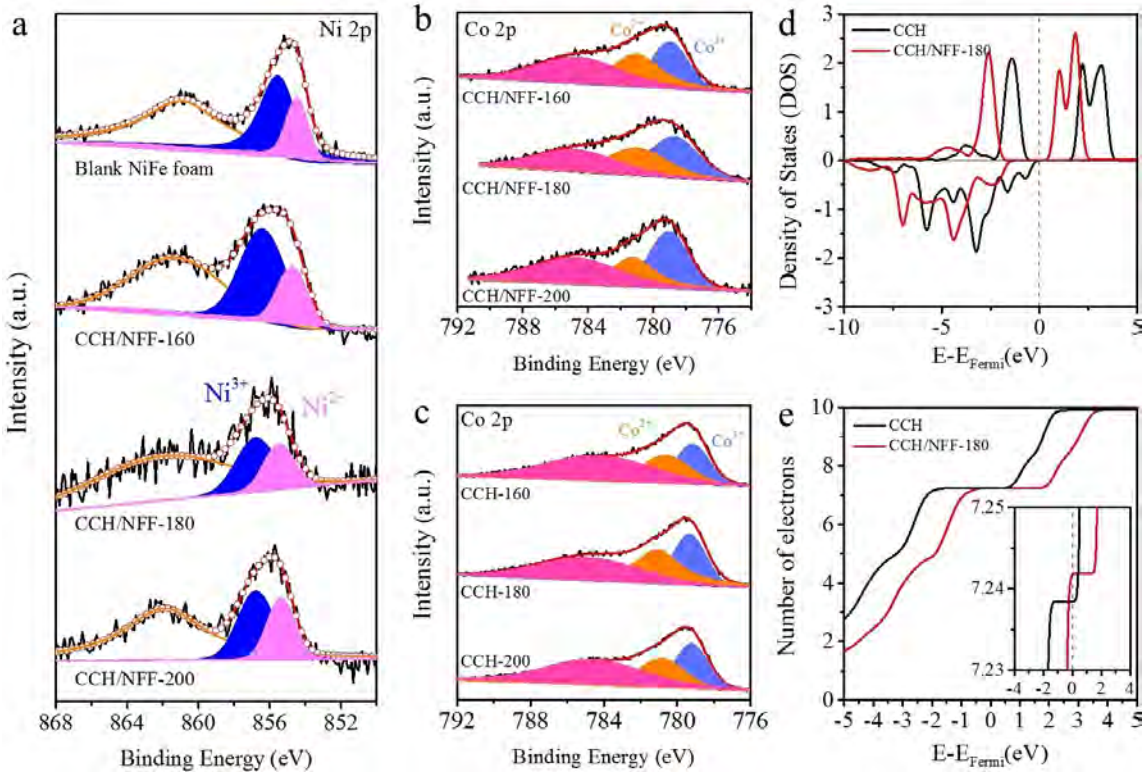

Figure 3. a) XPS spectra of Ni 2p for the different samples prepared at various temperatures. b) XPS spectra of Co 2p for b) CCH/NFF and c) pure CCH prepared at different temperatures. d) DOS of Co 3d orbital and e) corresponding number of electrons in the 3d orbital per Co atoms in pure CCH and CCH-180.

of H and facilitate the desorption of H on the surface for HER reaction.[31,33] In the alkaline OER process, OH^- is absorbed at the active center (M–OH), and the OH^- anion directly combines with M–OH to form the M–O intermediate and H_2O. The subsequent production of M–OOH species takes place before it decomposes into O_2. During this heterogeneous reaction, the formation of M–OOH has been considered the rate-limited step.[1] Compared with the pure CCH, the relative negative shift in the PDOS profile of CCH/NFF-180 demonstrates that the co-doping of Ni and Fe reduces the 3d orbital energy of Co and further enables Co to obtain more electrons. The exact electron transfer number between the metal cations could be obtained by integrating the DOS plots, as shown in Figure 3e. Compared with the pure CCH (the electron number of Co is around 7.238), the electron number of Co atoms in Ni and Fe co-doped CCH is around 7.242, consistent with the above XPS analysis. According to previous reports, the enhanced energy density of the active center is beneficial for the OOH species absorption.[34,35] Therefore, the increased 3d orbital electron density around Co facilitates the formation of absorbed OOH intermediates after Ni and Fe co-doping, thus improving the OER performance.

The electrochemical activities of these samples, including CCH/NFF-160, CCH/NFF-180, CCH/NFF-200, bare NiFe foam, and commercial RuO_2/NFF towards the OER were examined by obtaining representative iR-corrected polarization curves in a 1 M KOH, utilizing a standard three-electrode system. Figure 4a displays the cyclic voltammetry (CV) curves for OER. Bare NiFe foam shows the worst activity, suggesting the substrate is inactive for OER. After hydrothermal treatment at different temperatures, CCH/NFF-180 exhibited higher OER performance than other samples, including commercial RuO_2/NFF. Specifically, the activity performance follows the sequence: CCH/NFF-180 > CCH/NFF-160 > commercial RuO_2 > CCH/NFF-200 > bare NFF. In addition, to investigate the real active site of the CCH/NFF, the HMTA/NFF-180 (HMTA: hexamethylenetetramine) without $Co(NO_3)_2 \cdot 6H_2O$ was also fabricated with the hydrothermal method. The results show the performance of CCH/NFF-180 is still higher than that of HMTA/NFF-180, indicating Co plays an ignorable effect on the superior OER performance. Figure 4b and 4c provide detailed performance information, showing that CCH/NFF-180 displays the minimum overpotentials of 186 mV, 256 mV, and 277 mV at 10, 100, and 200 mV cm^{-2}, respectively. The excellent OER performance of CHH/NFF-180 is comparable to that of other OER catalysts (Table S4). For large-scale practical applications, we also investigate the overpotential needed for high current densities. The CCH/NFF-180 electrode requires only 309 and 340 mV overpotentials to obtain current densities of 500 and 1000 mA cm^{-2} compared to other samples. The effect of substrate types (Ni plate, Fe plate, Ni foam and Fe foam) on the catalyst activity were further discussed. As shown in Figure S5 and S6, the catalyst prepared on NiFe foam with 3D porous structure has the best OER activity. The results not only demonstrated that the 3D porous structure exposes more active sites, but also the co-doping of Ni and Fe on the CCH improves

© 2023 Wiley-VCH GmbH

18673899, 2024, 4, Downloaded from https://chemistry-europe.onlinelibrary.wiley.com/doi/10.1002/cctc.202301324 by City Universitaet Of Hong Kong, Wiley Online Library on [05/03/2024]. See the Terms and Conditions (https://onlinelibrary.wiley.com/terms-and-conditions) on Wiley Online Library for rules of use; OA articles are governed by the applicable Creative Commons License

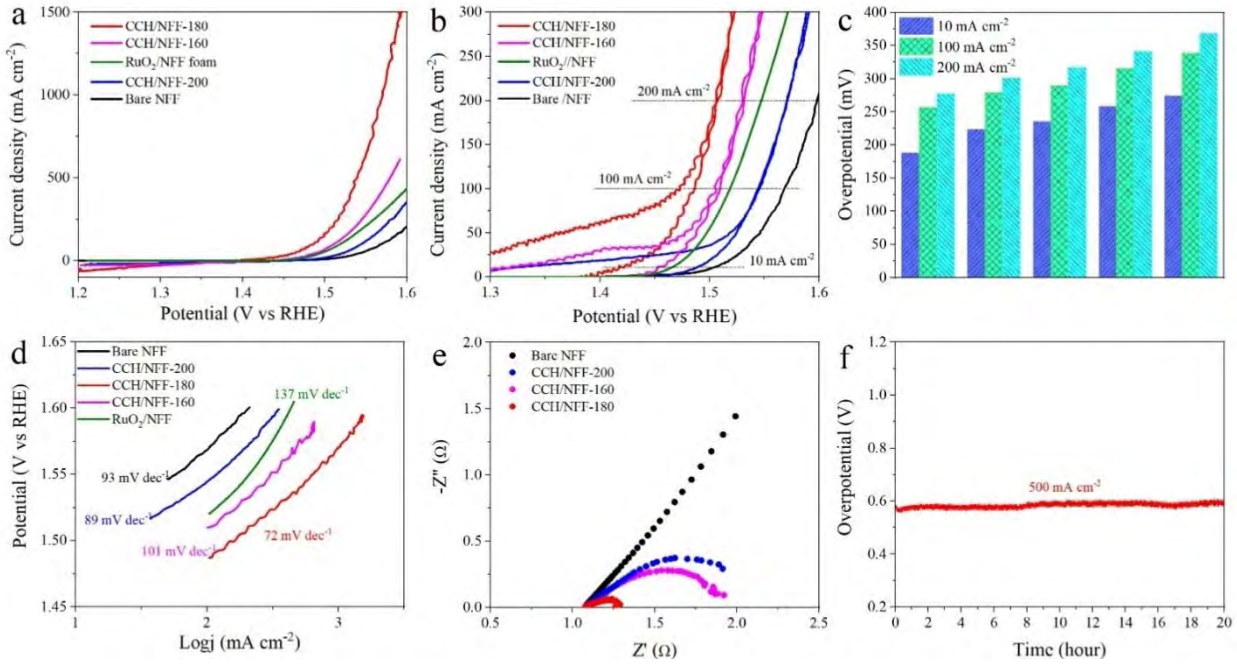

Figure 4. OER performance of CCH/NFF and RuO_2/NFF operated in 1 M KOH. a) Polarization curves and b) corresponding enlarged curves. c) Comparison of overpotentials needed at the current densities of 10, 100, and 200 mA cm^{-2}. d) Tafel slopes of CCH/NFF and RuO_2/NFF. e) Electrochemical impedance spectroscopy (EIS) for the samples. R1 and CPE is the electrolyte resistance and constant phase element, respectively. f) Chronopotentiometry curves of CCH-180 at constant current densities of 500 and 1000 mA cm^{-2}.

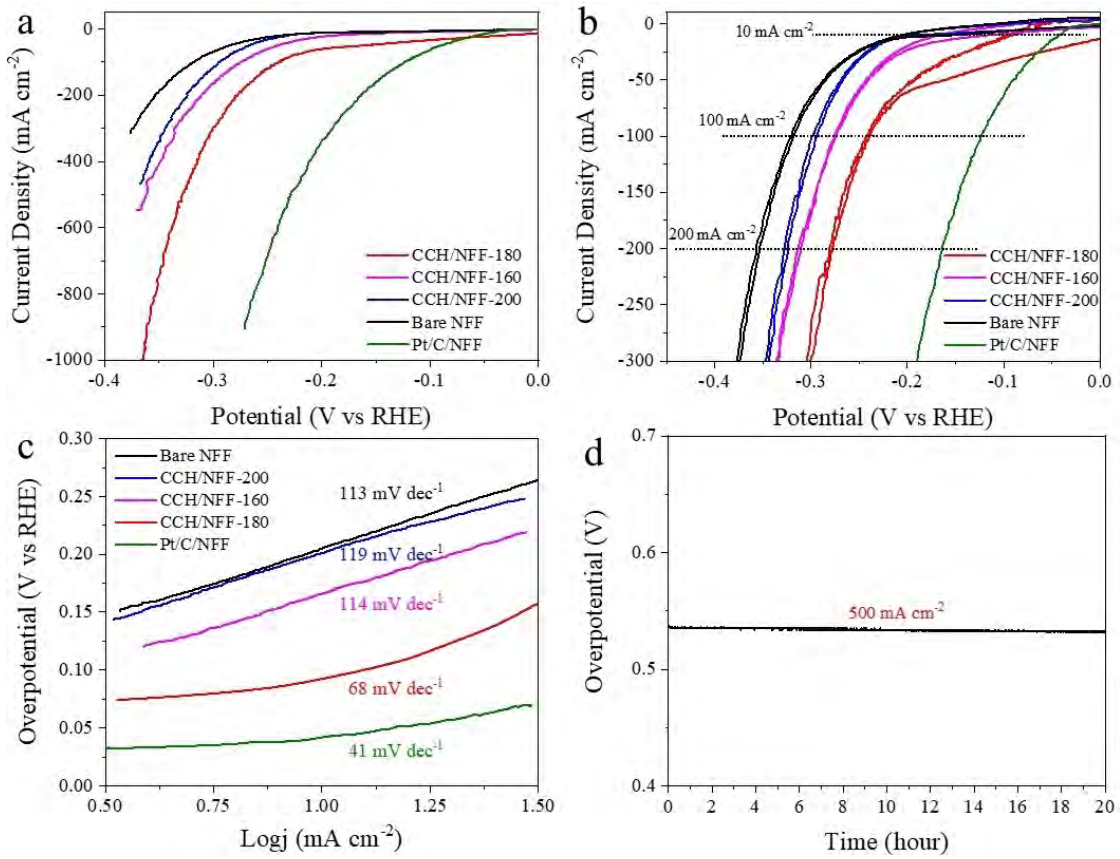

Figure 5. HER performance of CCH/NFF and Pt/C/NFF tested in 1 M KOH. a) and b) are the polarization curves recorded at scan rate 5 mV s^{-1}, and corresponding c) Tafel slopes. d) Chronopotentiometry curves of CCH/NFF-180 at constant current densities of 500 and 1000 mA cm^{-2}.

© 2023 Wiley-VCH GmbH

18673899, 2024, 4, Downloaded from https://chemistry-europe.onlinelibrary.wiley.com/doi/10.1002/cctc.202301324 by City Universitaet Of Hong Kong, Wiley Online Library on [05/03/2024]. See the Terms and Conditions (https://onlinelibrary.wiley.com/terms-and-conditions) on Wiley Online Library for rules of use; OA articles are governed by the applicable Creative Commons License

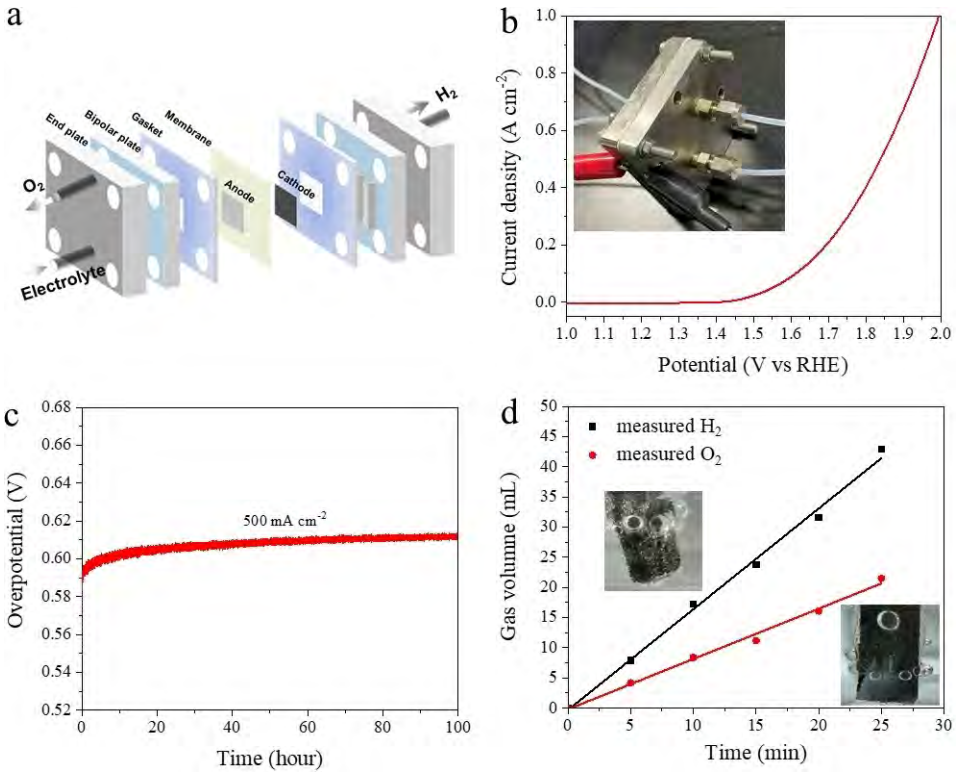

Figure 6. Overall water splitting performance of CCH/NFF-180. a) Schematic illustration of the water electrolyzer setup. b) LSV curves without iR correction and c) chronoamperometric curve at 500 mA cm^{-2} for 100 h. d) Experimental and theoretical amounts of H_2 and O_2 production by CCH/NFF-180 bifunctional electrocatalyst for overall water splitting.

the intrinsic activity of individual cobalt active sites compared to single element doping. In Figure 4d, the CCH/NFF-180 electrode also illustrates the minimal Tafel slope 72 mV dec^{-1} among these samples, in contrast to CCH/NFF-160 (101 mV dec^{-1}) and CCH/NFF-200 (89 mV dec^{-1}), which is even smaller than commercial RuO_2/NFF electrode (137 mV dec^{-1}), indicating the faster electron transfer progress and intrinsic high OER performance. In addition, electrochemical impedance spectroscopy (EIS) has been employed to investigate the kinetics of OER at the interface between the electrode and electrolyte, as shown in Figure 4e. The CCH/NFF-180 electrode has a much lower charge transfer resistance (R_{ct}) of 0.329 Ω, as compared to CCH/NFF-160 (0.565 Ω), CCH/NFF-200 (0.948 Ω) and bare NiFe substrate (2.671 Ω). The smallest R_{ct} of CCH/NFF-180 indicates desirable electron transport and catalytic kinetics, consistent with the Tafel slope.[36,37] Moreover, the CCH/NFF-180 electrode exhibits excellent stability during long-term electrochemical durability tests. As presented in Figure 4f, the overpotential required to achieve the current density of 500 mA cm^{-2} is about 0.57 V and exhibits negligible change after 20 h of operation, suggesting that CCH/NFF-180 is a promising candidate for large-scale practical application.

HER activities of the CCH/NFF electrode, along with the commercial Pt/C/NFF electrode, were then assessed in the 1 M KOH electrolyte (Figure 5a). As expected, the commercial Pt/C/NFF electrode exhibited the highest performance. In contrast, the CCH/NFF-180 electrode performs better than the CCH/NFF-160, CCH/NFF-200, and bare NiFe electrodes. At a current density of 10 mA cm^{-2}, the overpotential is only slightly greater than the 45 mV of the Pt/C/NFF electrode (Figure 5b). Specifically, this CCH/NFF-180 electrode can yield 10, 100, and 200 mA cm^{-2} with the overpotentials of 92, 240, and 280 mV, respectively (Figure 5b). In addition, the overpotentials of the CCH/NFF-180 electrode was 334 and 371 mV at current densities 500 and 1000 mA cm^{-2}, respectively. Furthermore, the Tafel plot based on the corresponding CV curve was used to investigate the HER kinetics (Figure 5c). Similarly, the effect of different substrates was analyzed on HER activity and the observed phenomenon is consistent with OER (Figure S7 and S8). The CCH/NFF-180 electrode has the smallest Tafel slope of 68 mV dec^{-1} besides Pt/C/NFF (41 mV dec^{-1}), which is lower than CCH/NFF-160 (114 mV dec^{-1}), CCH/NFF-200 (119 mV dec^{-1}) and bare NiFe electrodes (113 mV dec^{-1}), indicating a competitive advantage for practical applications. The electrochemical stability was further conducted on CCH/NFF-180 at a high current density, as shown in Figure 5d. As far as chronoamperometric durability test, at 500 mA cm^{-2}, a negligible decrease was observed in the overpotential after 20 h of operation.

Because of the exceptional electrochemical performance of CCH/NFF-180 towards OER and HER, an overall water splitting test was conducted by employing CCH/NFF-180 as both the cathode and anode in an anion exchange membrane-based water electrolyzer as shown in Figure 6a. The CCH/NFF-180 is capable of attaining a current density of 1000 A cm^{-2} at a voltage of 2 V (Figure 6b). The performance outperforms many non-noble bifunctional catalysts, as shown in Table S4. At the

© 2023 Wiley-VCH GmbH

18673899, 2024, 4, Downloaded from https://chemistry-europe.onlinelibrary.wiley.com/doi/10.1002/cctc.202301324 by City Universitaet Of Hong Kong, Wiley Online Library on [05/03/2024]. See the Terms and Conditions (https://onlinelibrary.wiley.com/terms-and-conditions) on Wiley Online Library for rules of use; OA articles are governed by the applicable Creative Commons License

same time, the CCH/NFF-180 electrode exhibits excellent stability after a long-term test of 100 h at a current density of 500 mA cm^{-2} (Figure 6c). Finally, gaseous products of the overall water splitting by the CCH/NFF-180 electrode were detected by gas chromatography. The volume ratio between H_2 and O_2 is nearly 1:2, indicating an almost 100% Faradaic efficiency, as shown in Figure 6d.

In conclusion, cobalt carbonate hydroxides co-doped with Ni and Fe were *in-situ* produced on the NiFe foam substrate by surface hydrothermal technique. It is worth noting that the dopant concentration and morphology on the catalyst can be conveniently modified by altering the hydrothermal temperature. Thus, based on various characterization techniques, the NiFe foam substrate provides the porous structure that enhances the exposed number of active sites and serves as the precursor of the dopants, which modifies the intrinsic activity of the active sites. In fact, the developed Ni and Fe co-doped cobalt carbonate/NiFe electrode shows superior OER and HER bifunctional electrocatalytic performance, where an alkaline electrolyzer can be constructed with these electrodes reaching a current density of 1000 mA cm^{-2} with a voltage around 2 V over a 100 h of operation. In summary, Ni and Fe co-doped cobalt carbonate/NiFe electrodes reveal potential commercial opportunities in overall water splitting. Furthermore, our study presents experimental evidence of the significant role of the catalyst substrate in the hydrothermal reaction, offering novel ideas for improving the catalyst performance.

Appendix A. Supplementary material

Supplementary data associated with this article can be found in the online version at:

Acknowledgements

This work is financially supported by the Shanghai Sailing Program (23YF1455000).

Conflict of Interests

The authors declare no conflict of interest.

Data Availability Statement

The data that support the findings of this study are available from the corresponding author upon reasonable request.

Keywords: *In-situ* co-doping · Cobalt Carbonate Hydroxides · Overall Water Splitting · Substrate Effect

[1] N.-T. Suen, S.-F. Hung, Q. Quan, N. Zhang, Y.-J. Xu, H. M. Chen, *Chem. Soc. Rev.* **2017**, *46*, 337–365.
[2] H. Over, *Chem. Rev.* **2012**, *112*, 3356–3426.
[3] M. Fang, G. Dong, R. Wei, J. C. Ho, *Adv. Energy Mater.* **2017**, *7*, 1700559–1700584.
[4] A. Mahmood, W. Guo, H. Tabassum, R. Zou, *Adv. Energy Mater.* **2016**, *6*, 1600423–1600446.
[5] S. Anantharaj, P. E. Karthik, B. Subramanian, S. Kundu, *ACS Catal.* **2016**, *6*, 4660–4672.
[6] J. Shan, C. Guo, Y. Zhu, S. Chen, L. Song, M. Jaroniec, Y. Zheng, S. Z. Qiao, *Chem.* **2019**, *5*, 445–459.
[7] Y. Wu, Y. Liu, G. D. Li, X. Zou, X. Lian, D. Wang, L. Sun, T. Asefa, X. Zou, *Nano Energy.* **2017**, *35*, 161–170.
[8] D. Senthil Raja, H. W. Lin, S. Y. Lu, *Nano Energy.* **2019**, *57*, 1–13.
[9] X. Cheng, Z. Pan, C. Lei, Y. Jin, B. Yang, Z. Li, X. Zhang, L. Lei, C. Yuan, Y. Hou, *J. Mater. Chem. A.* **2019**, *7*, 965–971.
[10] C. Hu, L. Zhang, Z. J. Zhao, A. Li, X. Chang, J. Gong, *Adv. Mater.* **2018**, *30*, 1705538–1705546.
[11] Z. W. Seh, J. Kibsgaard, C. F. Dickens, I. Chorkendorff, J. K. Nørskov, T. F. Jaramillo, *Science.* **2017**, *355*, 146–158.
[12] R. Wei, X. Bu, W. Gao, R. A. B. Villaos, G. MacAm, Z. Q. Huang, C. Lan, F. C. Chuang, Y. Qu, J. C. Ho, *ACS Appl. Mater. Interfaces.* **2019**, *11*, 33012–33021.
[13] X. Liu, W. Xi, C. Li, X. Li, J. Shi, Y. Shen, J. He, L. Zhang, L. Xie, X. Sun, P. Wang, J. Luo, L. M. Liu, Y. Ding, *Nano Energy.* **2018**, *44*, 371–377.
[14] J. Hao, W. Yang, J. Hou, B. Mao, Z. Huang, W. Shi, *J. Mater. Chem. A.* **2017**, *5*, 17811–17816.
[15] J. Zhang, W. Xiao, P. Xi, S. Xi, Y. Du, D. Gao, J. Ding, *ACS Energy Lett.* **2017**, *2*, 1022–1028.
[16] S. Gao, G. D. Li, Y. Liu, H. Chen, L. L. Feng, Y. Wang, M. Yang, D. Wang, S. Wang, X. Zou, *Nanoscale.* **2015**, *7*, 2306–2316.
[17] Y. P. Zhu, Y. Jing, A. Vasileff, T. Heine, S. Z. Qiao, *Adv. Energy Mater.* **2017**, *7*, 1602928–1602936.
[18] W. Gao, M. Yan, H. Y. Cheung, Z. Xia, X. Zhou, Y. Qin, C. Y. Wong, Y. Qu, C. R. Chang, J. C. Ho, *Nano Energy.* **2017**, *38*, 290–296.
[19] C. Liu, G. Zhang, L. Yu, J. Qu, H. Liu, *Small.* **2018**, *14*, 1800421–1800430.
[20] X. Bu, R. Wei, W. Gao, C. Lan, J. C. Ho, *J. Mater. Chem. A.* **2019**, *7*, 12325–12332.
[21] Z. Cai, X. Bu, P. Wang, W. Su, R. Wei, J. C. Ho, J. Yang, X. Wang, *J. Mater. Chem. A.* **2019**, *7*, 21722–21729.
[22] T. Tang, W. J. Jiang, S. Niu, N. Liu, H. Luo, Y. Y. Chen, S. F. Jin, F. Gao, L. J. Wan, J. S. Hu, *J. Am. Chem. Soc.* **2017**, *139*, 8320–8328.
[23] P. Giannozzi, S. Baroni, N. Bonini, M. Calandra, R. Car, C. Cavazzoni, D. Ceresoli, G. L. Chiarotti, M. Cococcioni, I. Dabo, A. Dal Corso, S. De Gironcoli, S. Fabris, G. Fratesi, R. Gebauer, U. Gerstmann, C. Gougoussis, A. Kokalj, M. Lazzeri, L. Martin-Samos, N. Marzari, F. Mauri, R. Mazzarello, S. Paolini, A. Pasquarello, L. Paulatto, C. Sbraccia, S. Scandolo, G. Sclauzero, A. P. Seitsonen, A. Smogunov, P. Umari, R. M. Wentzcovitch, *J. Phys. Condens. Matter.* **2019**, *21*, 395502–395521.
[24] M. B. P Giannozzi, O Andreussi, T Brumme, O Bunau, M. C. Nardelli, M Calandra, R Car, C Cavazzoni, D Ceresoli, S. de G. N Colonna, I Carnimeo, A Dal Corso, G. F. P Delugas, R A DiStasio Jr, A Ferretti, A Floris, J. J. G Fugallo, R Gebauer, U Gerstmann, F Giustino, T Gorni, M. L. M Kawamura, H–Y Ko, A Kokalj, E Küçükbenli, H.-V. N. M Marsili, N Marzari, F Mauri, N L Nguyen, R. S. A Otero-de-la-Roza, L Paulatto, S Poncé, D Rocca, I. T. B Santra, M Schlipf, A P Seitsonen, A Smogunov, X. W., S. B. T. Thonhauser, P Umari, N Vast, *J. Phys. Condens. Matter.* **2017**, *29*, 465901–465931.
[25] S. Grimme, J. Antony, S. Ehrlich, H. Krieg, *J. Chem. Phys.* **2010**, *132*, 154104–154123.
[26] J. M. Smith, S. P. Jones, L. D. White, *Phys. Rev. B.* **1990**, *41*, 7892–7895.
[27] K. Lejaeghere, G. Bihlmayer, T. Björkman, P. Blaha, S. Blügel, V. Blum, D. Caliste, I. E. Castelli, S. J. Clark, A. Dal Corso, S. De Gironcoli, T. Deutsch, J. K. Dewhurst, I. Di Marco, C. Draxl, M. Dułak, O. Eriksson, J. A. Flores-Livas, K. F. Garrity, L. Genovese, P. Giannozzi, M. Giantomassi, S. Goedecker, X. Gonze, O. Grånäs, E. K. U. Gross, A. Gulans, F. Gygi, D. R. Hamann, P. J. Hasnip, N. A. W. Holzwarth, D. Iuşan, D. B. Jochym, F. Jollet, D. Jones, G. Kresse, K. Koepernik, E. Küçükbenli, Y. O. Kvashnin, I. L. M. Locht, S. Lubeck, M. Marsman, N. Marzari, U. Nitzsche, L. Nordström, T. Ozaki, L. Paulatto, C. J. Pickard, W. Poelmans, M. I. J. Probert, K. Refson, M. Richter, G. M. Rignanese, S. Saha, M. Scheffler, M. Schlipf, K. Schwarz, S. Sharma, F. Tavazza, P. Thunström, A. Tkatchenko, M. Torrent, D. Vanderbilt, M. J. Van Setten, V. peybroeck, J. M. Wills, J. R. Yates, G. X. Zhang, S. Cottenier, *Science.* **2016**, *351*, 1415–1423.
[28] Q. He, Y. Wan, H. Jiang, Z. Pan, C. Wu, M. Wang, X. Wu, B. Ye, P. M. Ajayan, L. Song, *ACS Energy Lett.* **2017**, *2*, 1373–1380.

© 2023 Wiley-VCH GmbH

18673899, 2024, 4, Downloaded from https://chemistry-europe.onlinelibrary.wiley.com/doi/10.1002/cctc.202301324 by City Universitaet Of Hong Kong, Wiley Online Library on [05/03/2024]. See the Terms and Conditions (https://onlinelibrary.wiley.com/terms-and-conditions) on Wiley Online Library for rules of use; OA articles are governed by the applicable Creative Commons License

[29] K. Zhu, T. Wu, Y. Zhu, X. Li, M. Li, R. Lu, J. Wang, X. Zhu, W. Yang, *ACS Energy Lett.* **2017**, *2*, 1654–1660.
[30] S. Sun, H. Li, Z. J. Xu, *Joule.* **2018**, *2*, 1024–1027.
[31] Z. Chen, Y. Song, J. Cai, X. Zheng, D. Han, Y. Wu, Y. Zang, S. Niu, Y. Liu, J. Zhu, X. Liu, G. Wang, *Angew. Chemie Int. Ed.* **2018**, *57*, 5076–5080.
[32] J. H. Kim, D. H. Youn, K. Kawashima, J. Lin, H. Lim, C. B. Mullins, *Appl. Catal. B Environ.* **2018**, *225*, 1–7.
[33] B. Hammer, J. K. Nørskov, *Adv. Catal.* **2000**, *45*, 71–129.
[34] S. Zhao, R. Jin, H. Abroshan, C. Zeng, H. Zhang, S. D. House, E. Gottlieb, H. J. Kim, J. C. Yang, R. Jin, *J. Am. Chem. Soc.* **2017**, *139*, 1077–1080.
[35] Y. R. Zheng, M. R. Gao, Z. Y. Yu, Q. Gao, H. L. Gao, S. H. Yu, *Chem. Sci.* **2011**, *6*, 4594–4598.
[36] R. Wei, M. Fang, G. Dong, C. Lan, L. Shu, H. Zhang, X. Bu, J. C. Ho, *ACS Appl. Mater. Interfaces.* **2018**, *10*, 7079–7086.
[37] X. Liang, R. Dong, D. Li, X. Bu, F. Li, L. Shu, R. Wei, J. C. Ho, *ChemCatChem.* **2018**, *10*, 4555–4561.

Manuscript received: October 20, 2023
Revised manuscript received: December 13, 2023
Accepted manuscript online: December 22, 2023
Version of record online: January 22, 2024

© 2023 Wiley-VCH GmbH

18673899, 2024, 4, Downloaded from https://chemistry-europe.onlinelibrary.wiley.com/doi/10.1002/cctc.202301324 by City Universitaet Of Hong Kong, Wiley Online Library on [05/03/2024]. See the Terms and Conditions (https://onlinelibrary.wiley.com/terms-and-conditions) on Wiley Online Library for rules of use; OA articles are governed by the applicable Creative Commons License